Received: 16 September 2025 | Revised: 24 October 2025 | Accepted: 28 October 2025

DOI: 10.1002/rpm2.70027

RESEARCH ARTICLE

RESPONSIVE MATERIALS Open Access WILEY

Photo-regenerable liquid crystalline polymers for the adsorption of organic pollutants

Valeria D'Agostino[1] | Vincenzo Spinoso[2] | Giusy Curcuruto[3] | Alessandra Longo[3] | Alejandro Martinez-Bueno[2,4] | Andrea Lanfranchi[5] | Chiara Laferrera[6] | Giuliana Impellizzeri[6] | Paola Lova[5] | Martina Salzano de Luna[1] | Daniele Martella[2,4]

[1]Department of Chemical, Materials and Production Engineering (INSTM Consortium – UdR Naples), University of Naples Federico II, Naples, Italy

[2]European Laboratory for Non-Linear Spectroscopy (LENS), University of Florence, Sesto Fiorentino, Italy

[3]CNR-IPCB, Catania, Italy

[4]Department of Chemistry, University of Florence, Sesto Fiorentino, Italy

[5]Department of Chemistry and Industrial Chemistry, University of Genoa, Genoa, Italy

[6]CNR-IMM, Catania, Italy

Correspondence

Alejandro Martinez-Bueno and Andrea Lanfranchi.
Email: alejandro.martinezbueno@unifi.it and andrea.lanfranchi@edu.unige.it

Abstract

The increasing presence of organic pollutants such as herbicides and pesticides in water, soil and air requires efficient strategies for their removal and degradation in a reliable and environmentally sound manner. This work focuses on adsorbent materials for water remediation, also addressing pollutant degradation, a critical aspect allowing adsorbent re-use. A photo-regenerable adsorbent based on a liquid crystal network (LCN) is proposed, consisting of a highly ordered nanoporous material obtained through the polymerization of reactive mesogenic monomers. The addition of titanium dioxide nanoparticles in the LCN matrix as photocatalyst opens to its photoregeneration, allowing degradation of the pollutants and further cycles of adsorption. The LCN-TiO_2 composite was optimized using methylene blue (MB) as a model and then tested for a real pollutant. The adsorber proved its efficiency with a maximum pollutant uptake of 86 wt% and total photoregeneration achieved by irradiation with an ultraviolet source. The best tradeoff of adsorption capacity and photoregeneration efficacy was found for samples loaded with only 1 wt% of TiO_2 nanoparticles. This composite also exhibited a high pollutant adsorption capacity and fast and complete photo-regeneration toward the herbicide Diquat, opening the way for a new versatile strategy for water remediation from emerging organic pollutants.

Keywords

adsorption, liquid crystal networks, photocatalysis, regeneration, water remediation

1 | INTRODUCTION

The XXI century has been identified as "the century of the environment,"[1] with the intent to highlight the increasing global concerns related to the growing pollution due to human activity, and the urgent need for a robust contribution from the scientific community to tackle this issue.[1–5] According to the new European Policies of Circular Economy, water management is no more just a matter of wastewater disposal, but it is steadily shifting towards considering it as a resource.[6] Henceforth, developing new strategies to remove contaminants is an ongoing challenge driven by the increasing release of harmful substances resulting from human activities. To this end, in addition to secondary treatment technologies, further decontamination processes need to be included in the purification line for wastewater to be

Valeria D'Agostino and Vincenzo Spinoso contributed equally to this work.

reused, with the purpose of reducing the amount of emerging and persistent pollutants.[2] This step is particularly important in the presence of emerging organic contaminants,[2–5] that are synthetic organic chemicals (such as pharmaceuticals[7,8] and personal care products,[9] endocrine disrupting chemicals,[10] and pesticides[11]), for which established detoxification strategies are still missing. Indeed, their presence in water even at low concentration (from ng L^{-1} up to mg L^{-1}) is raising serious concerns regarding the potential threat to natural ecosystems and human health.[4,7,12,13]

Among removal strategies, adsorption is claimed as one of the most feasible, versatile and low-cost methods, relying on physical and/or chemical interactions between the targeted molecules and the adsorbing substrate.[3,13–15] With respect to other methods such as advanced oxidation,[16] adsorption via films eliminate the need to remove the oxidizer from the clean water, whereas they in principle require less energy compared to membrane processes.

In the field of pollutants adsorption, nanoporous self-assembled polymers have attracted increasing attention thanks to their tunable molecular design, which also allows selectivity toward specific pollutants, depending on their size and/or charge.[17,18] Within this context, liquid crystals (LCs) are especially interesting materials, with great versatility of use spanning from electro-actuable systems[19,20] or batteries[21] with the possibility of working with chiral systems[22,23] and overall in the field of responsive materials.[24–27] Specifically, liquid crystal networks (LCNs) represent one of the main classes of materials for designing highly ordered nanoporous adsorbent suitable for molecular separation.[28–36] A distinctive advantage of these systems relies in their ability to preserve the orientational order of the liquid crystalline phase upon polymerization,[28] while nanoporosity can be introduced by either disruption of non-covalent interactions (e.g., hydrogen bonds) or by the selective removal of porogenic templates.[30,31] Among the different liquid crystalline organizations, smectic phases offer several advantages for the preparation of adsorbent LCNs. Their molecular design typically relies on simple, linear mesogenic units that are easier to synthesize and purify compared to those required for more complex structures like columnar or cubic. Moreover, smectic phases exhibit well-defined lamellar ordering combined with higher fluidity, enabling easier processing and alignment of monomers prior to polymerization. These features allow the formation of highly ordered films with controllable orientation and charge and size selective adsorption, as demonstrated by Schenning and coworkers.[30,37]

However, these materials are hardly re-usable as pollutants cannot be degraded or eliminated.[33,34] In this regard, integrated photocatalytic adsorbents exploiting wide energy gap semiconductors to oxidize adsorbed pollutants to carbon dioxide and water upon light absorption would represent a significant advancement. To date, most photocatalytic adsorbents have been developed in powder form. Among these, different researches reported on titanium dioxide–zeolite hybrids,[38,39] metal oxide–supported activated carbons,[40,41] and ZnO/clay nanoarchitectures, or even 2D materials such as planar carbon nitride[42,43] with good degradation rates.[44,45] Powders have some advantages with respect to films catalysts thanks to their greater surface area and large surface/volume ratio, which in turn positively affects the reaction kinetics.[46,47] Nonetheless, the recovery of powders after treatment, typically by filtration or decantation, remains time and energy intensive thus limiting their large scale applicability.[4,44,48–50]

Our work fits this general framework, as it presents a novel photocatalytic adsorbent based on an LCNs composite film loaded with titania nanoparticles. Figure 1 schematizes the working principle of the system as well as its composition. The smectic phase of the LCN takes up the role of adsorber, whereas the TiO_2 nanoparticles, embedded in the film, provide the needed photocatalytic properties without altering consistently the adsorption capacity. This way, the system can effectively adsorb pollutants thanks to the LCN smectic structure, and those pollutants are afterward degraded upon UV irradiation. In addition to high sorption capacity, the use of LCN allows for adsorption selectivity. Indeed, alkaline treatment of the LCN breaks hydrogen bonds, generating porosity and exposing carboxylate groups, which enable the selective adsorption of cationic organic pollutants from water. Upon UV illumination, the TiO_2 nanoparticles generate reactive oxygen species (ROS) that oxidize the adsorbed pollutants into smaller intermediates and eventually harmless products such as CO_2 and H_2O, allowing multiple adsorption–desorption cycles. The adsorption selectivity toward cationic species, adsorption capacity, photocatalytic activity and reusability were first evaluated using methylene blue (MB) as a model pollutant. Afterward, promising results were obtained in the adsorption

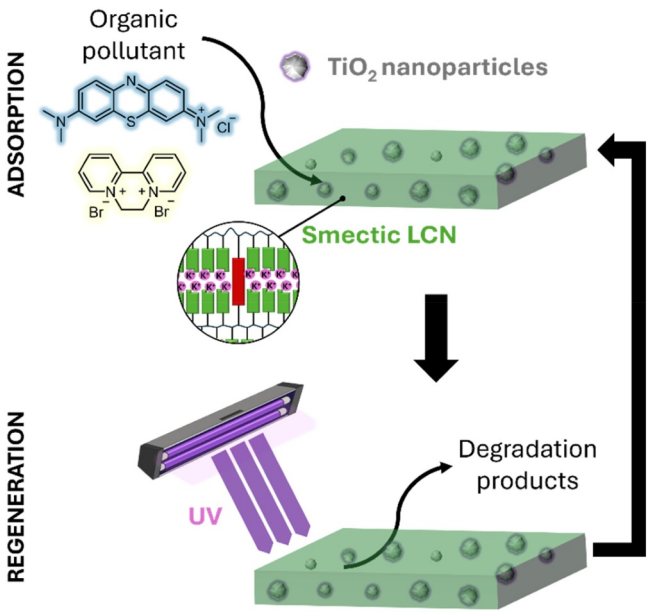

FIGURE 1 Schematic of the use of TiO_2-loaded LCNs for water remediation. LCNs, liquid crystal networks.

and degradation of a real organic pollutant, Diquat, a widely used herbicidal agent.[51,52] While previous studies have reported LCN-based adsorbents or TiO_2 photocatalysts for water remediation, our approach combines the structural organization of smectic LCNs with the photocatalytic properties of titania nanoparticles in a single system. This design allows simultaneous selective adsorption of cationic pollutants and in situ photocatalytic degradation, overcoming the limitations that both systems have when used separately.

2 | RESULTS AND DISCUSSION

2.1 | LC mixtures and LCNs

Prior to polymerization, we assessed the effect of TiO_2 nanoparticles on the thermal properties and phase behavior of the LC monomer mixture performing a polarized optical microscopy (POM) observation upon heating. The pristine LC mixture revealed a first melting at ~90°C and a transition to the isotropic phase (clearing point) at ~110°C (Figure S1, black dot micrograph). Upon cooling, a Schlieren texture typical of nematic mesophases appeared at ~110°C (yellow dot), which evolved into a fan-shaped texture below 100°C (red dot), indicating the formation of a smectic phase.[26,53] Further cooling led to crystallization of the sample at ~60°C (green dot). This thermal behavior is consistent with the differential scanning calorimetry (DSC) thermogram (Figure S1, upper left, and upper right for the magnification of high-temperature-region), which showed during the heating cycle a large endothermic peak at 91°C and two smaller endothermic events at 101°C and 108°C, corresponding to the transitions from the crystalline phase to the smectic phase, from the smectic to the nematic phase, and from the nematic phase to the isotropic liquid, respectively.[30,54–56] TiO_2 addition (1–10 wt%) preserved the general mesomorphic phase behavior and transition temperatures (Figures S2–S4 and Table S1), with all mixture presenting the smectic phase useful to prepare the nanoporous LCN.[57] However, POM analysis revealed a progressive increase in nanoparticle aggregates that interfered with the optical homogeneity of the films and masked the underlying liquid crystalline textures. Upon polymerization (Section 4 and Figure 2a,b), POM images confirm that the TiO_2 nanoparticles were distributed throughout the entire films (Figure S5 and digital photographs in Figure 2c). The completion of polymerization was verified via attenuated total reflectance infrared (ATR-IR), where the disappearance of characteristic acrylate band at 804 cm^{-1} confirmed the consumption of reactive acrylate double bonds (Figure 2d, blue and black curves, and Figure S6). DSC analysis on the polymerized pristine LCN film shows only a glass transition temperature (T_g) around 70°C (Figure S7).

To cleave the hydrogen bonds associated with the carboxylic acid groups and activate the adsorber, the films were immersed in an aqueous solution of KOH. ATR-IR spectra collected before and after the treatment reveal the shift of the C=O stretching band from 1676 cm^{-1} (characteristic of carboxylic acid dimers),[58] to 1542 cm^{-1}, indicating the disruption of the hydrogen bonds and the formation of the carboxylate salt (Figure 2d, black and red curves, and Figure S8).[30,58] The complete disappearance of the band at 1676 cm^{-1} confirm that all carboxylic acid groups have been deprotonated, evidencing the full cleavage of the intermolecular hydrogen bonds. Further confirmation of this is given by the adsorption of MB after different times of immersion in KOH (see following section).

2.2 | Adsorption properties of LCNs

The presence of carboxylate moieties in the LCN allows selective removal of cationic species as demonstrated by the adsorption tests in solutions containing both anionic and cationic molecules. Figure 3a,b reports the UV-Vis spectra of binary dye solutions before and after LCN addition. In particular in Figure 3a, a mixture of Indigo Carmine and Rhodamine 6G shows the absorbance peak of both Rhodamine (cationic, λ_{max} = 526 nm) and Indigo Carmine (anionic, λ_{max} = 609 nm). After placing the LCN in the mixture for 48 h the peak corresponding to Rhodamine 6G is no longer visible (blue line), proving its efficient removal. To verify that this process is not dye-specific, the same test was performed for another dye pair, that is a mixture of MB (cationic, λ_{max} = 662 nm) and Methyl Orange (anionic, λ_{max} = 464 nm) with analogous results. Indeed, when adsorption takes place, the peak at 662 nm completely disappears, while the peak at 465 nm, assigned to the anionic Methyl Orange, remains essentially unaltered (Figure 3b).

The adsorption behavior of the LCN samples was quantified by performing adsorption isotherms for MB as a prototype pollutant. Figure 3c shows six MB solutions at increasing concentrations (left to right) before and after the adsorption process, showing that LCN can completely remove the dye molecules up to a threshold value. A typical adsorption kinetics is reported in Figure S9. Figure 3d reports the equilibrium adsorption capacity calculated according to Equation (1) as a function of the equilibrium residual dye concentration. For all the films, the adsorption behavior nicely follows the Langmuir isotherm model:

$$q_e = q_L \frac{k_L C_e}{1 + k_L C_e} \quad (1)$$

where k_L is the Langmuir constant related to adsorbent/adsorbate affinity and q_L represents the maximum adsorption capacity (fitting parameters are reported in Table S2).[59] Langmuir-type isotherms suggest that the adsorption of MB molecules primarily occurs through monolayer coverage on a homogeneous surface with uniformly distributed adsorption sites, which is in line with the molecular arrangement sketched in Figure 2a for LCN films after KOH treatment. The calculated q_L value for the pristine film (~865 mg g^{-1}) is

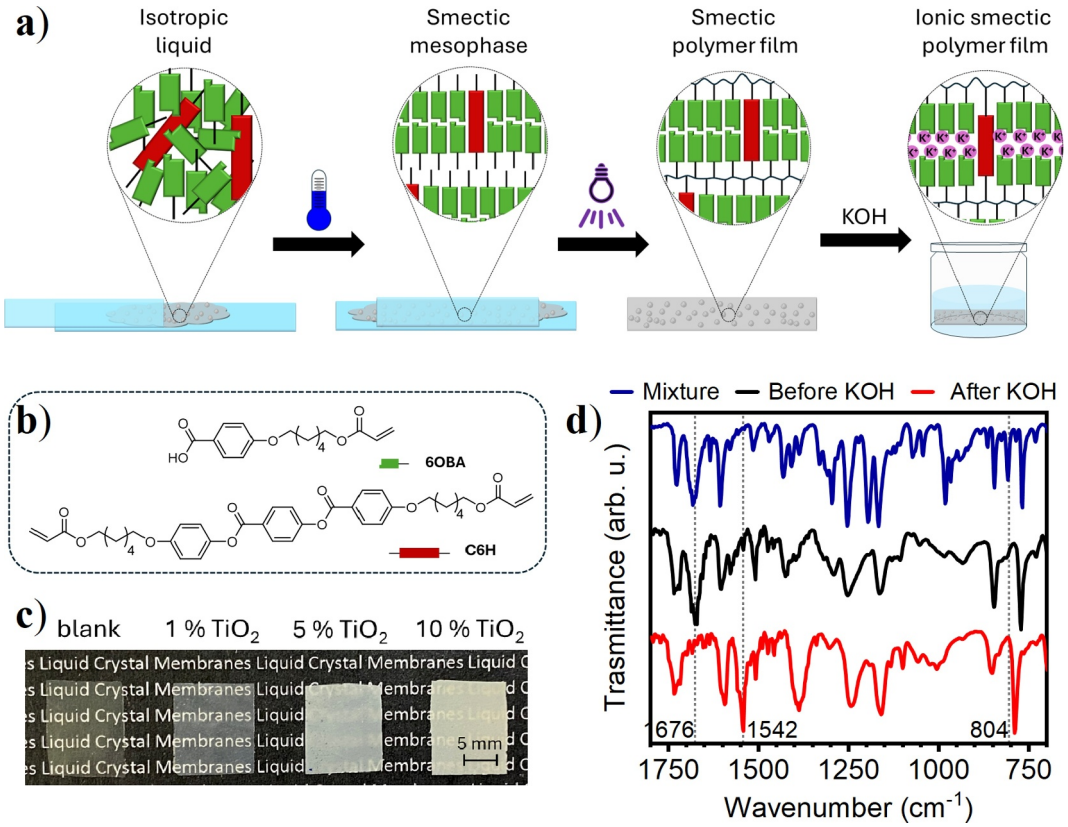

FIGURE 2 (a) Schematic representation of material preparation (green: monomer, red: crosslinker); (b) Structure formula of the monomer (6OBA) and the crosslinker (C6H); (c) Photographs of free-standing films; (d) Attenuated total reflectance infrared spectra of the liquid crystal mixture, polymerized film and the KOH-treated film.

in line with the maximum adsorption capacity report for other liquid crystalline membranes.[30]

The addition of TiO_2 barely lowers the maximum adsorption capacity, with an effect rather independent on the actual nanoparticle loading (Figure 3e). This result suggests that TiO_2 nanoparticles provide a limited contribution to MB adsorption possibly shielding the active sites of the LCN films and thus reducing their overall availability for adsorption.[60] Despite this modest detrimental effect, the calculated q_L values for the TiO_2-filled films are still rather high, in the range 740–760 mg g^{-1}, hence close to values obtained via the use of chitosan or nanocellulose and one order of magnitude greater than other membrane systems.[61,62] These high values (albeit expected to worsen slightly in nonpure water, due to the presence of competing ions[47]) makes LCN promising materials for effective combined adsorption and photocatalysis of organic pollutants.

Additionally, to gain a molecular-level understanding of the pollutant–LCN interactions, FTIR spectra were recorded for the carboxylated LCN before and after MB adsorption, along with that of pristine MB (Figure S10). The carbonyl stretching band of the carboxylic groups in the polymer, observed at ν (C=O) = 1730 cm^{-1} for the COO^-K^+ form (black line), shifted slightly to 1727 cm^{-1} upon interaction with MB (cyan line), evidencing perturbation of the carboxylate environment due to electrostatic pairing with the cationic dye. Concurrently, the symmetric C–H stretching vibration of the cationic dimethylamino groups of MB, located at ν_s (C–H) = 1387 cm^{-1} in the free dye (blue line), shifted to 1377 cm^{-1} (cyan line) when adsorbed on the LCN, further supporting the presence of ionic interactions between positively-charged MB and the carboxylate sites of the polymer. These correlated shifts confirm that adsorption primarily arises from electrostatic coupling rather than weak physisorption. Furthermore, measurements of MB adsorption after different total time of immersion in KOH (reported in Figure S11) seem to confirm this view. Indeed, while for a reduced concentration of MB (30 mg mL^{-1}, black line) no difference in adsorption capacity can be observed, for a higher concentration of 500 mg mL^{-1} there is a strong difference in adsorption capacity between the 15 min KOH-treated sample and the 1 h-treated one. In detail, only 60% of MB is adsorbed in the first case with respect to the latter.

2.3 | Photoregeneration of the LCNs

To test the possibility to re-use LCNs in multiple adsorption cycles, the samples were placed in MB solution with concentration typical of environmental pollutants (~1.2 ppm) for 3.5 h and then irradiated with the 365 nm LED. During irradiation, the peak absorbance associated with the MB was

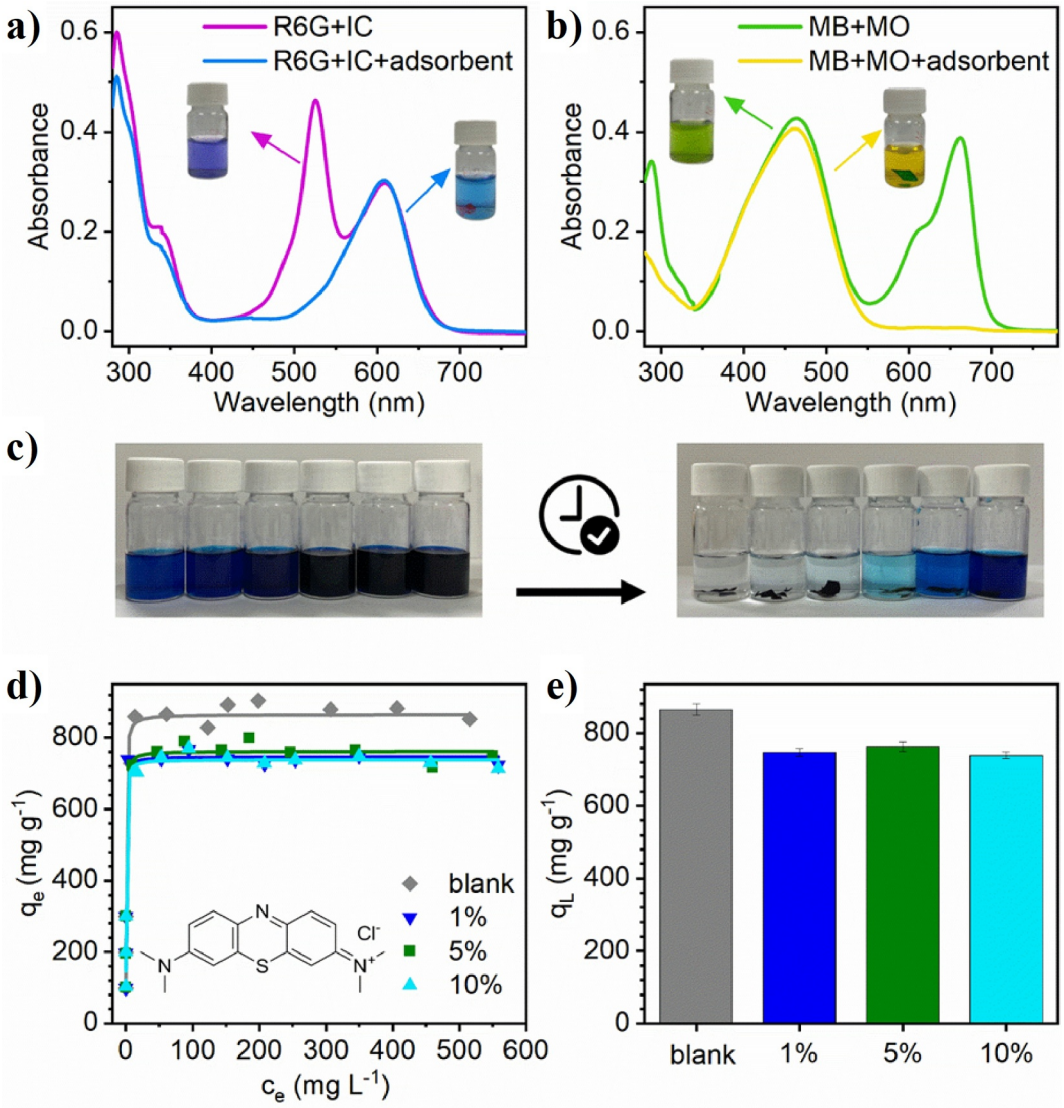

FIGURE 3 Adsorption properties of LCNs. (a, b) UV-vis spectra of binary dye solutions before and after adsorption: (a) RH + IC and (b) MB + MO. (c) Methylene Blue solutions before (left) and after (right) the adsorption process with LCN films. (d) Adsorption isotherms for pristine and the TiO_2-loaded LCN films with MB. Solid lines correspond to the best fitting of the Langmuir model (Equation S1) for experimental data. (e) Maximum adsorption capacity (q_L) for pristine and the TiO_2-loaded LCN films. IC, Indigo Carmine; LCNs, liquid crystal networks; MB, methylene blue; MO, methyl orange; RH, Rhodamine 6G.

monitored. The digital photographs of the samples before and after the regeneration and the dynamic of the peak intensity normalized for the initial value are reported in Figure 4a,b, respectively. The absorbance of the pristine LCN film (red lines in Figure 4a,b) shows a consistent decrease up to ~40% in 3 h. This behavior is assigned to the photobleaching of dye under irradiation, well-known in the field.[63–65] The sample with 1 wt% loading of titania (black lines in Figure 4a,b) shows a faster kinetic overall, with a slower rate than the samples with larger loads within the first 1.2 h. Then, the absorbance drops below 65% within 3 h. Notice that at this time the steady state has not been reached yet, suggesting that complete regeneration of the sample is slow but possible (see data for longer exposure in Figure 4c, black line). The samples with 5 wt% and 10 wt% TiO_2 loading (green and blue lines in Figure 4a,b) show an equilibrium value at around 50% of the initial absorbance. The behavior observed can also be seen in the digital photograph of the samples in Figure 4a, where only for 1 wt% TiO_2 sample, the blue color is no longer visible to the naked eye.

Such results depend on the interplay of photocatalytic effect, photobleaching, and scattering: large TiO_2 concentration are highly photocatalytic but cause consistent scattering (see Figure 2c as reference). Because the samples are irradiated from a single side (i.e., the bottom surface), the degradation kinetic in the lower part of the sample is fast (hence the rapid initial decrease in absorbance) but slow in the other (light cannot penetrate effectively through the whole sample). To confirm this interpretation, we performed

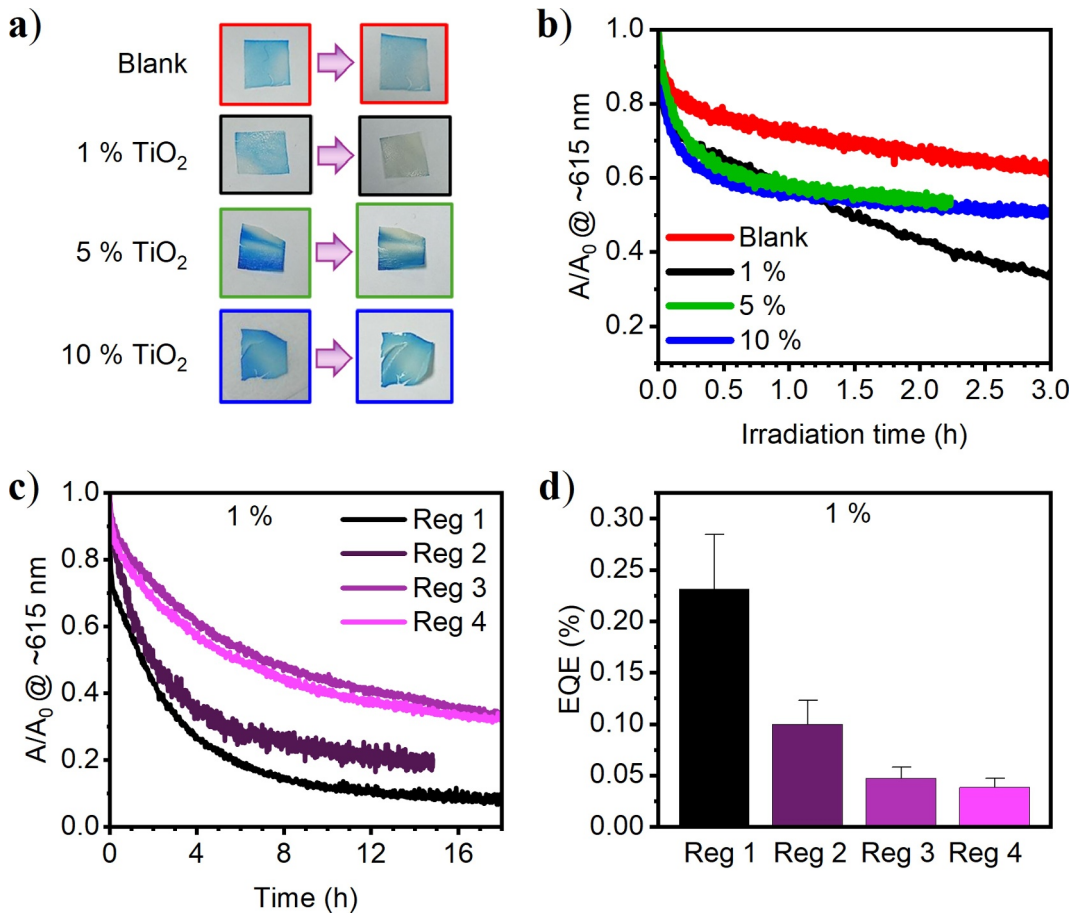

FIGURE 4 (a) Digital photographs of samples with different TiO_2 loadings before and after the regeneration. (b) Normalized absorbance (~615 nm) dynamics for the samples without TiO_2 (red curve), with 1 wt% TiO_2 (black curve) with 5% TiO_2 (blue curve), and 10% TiO_2 (green curve), collected during regeneration. (c) Normalized absorbance dynamics for the 1 wt% TiO_2 sample over following regeneration ("Reg") cycles (blue to lilac). (d) External quantum efficiency of the photoregeneration over progressive regeneration cycles.

a test raising the LED power to 100 mW cm^{-2}. In this situation (Figure S12), the samples containing 5 wt% and 10 wt% TiO_2 show the fastest kinetics and lower absorbance intensity values at the end of the irradiation. Conversely, the 1 wt% sample performs slightly worse than the reference in terms of both kinetic and amount of degraded dye. This behavior can be explained as photobleaching and photocatalysis are competitive processes and suggest that, at such intensity, the first process is dominant. However, because this intensity is very far from solar irradiation, which is most appealing for photodegradation, we kept the power at 19 mW cm^{-2} for the following tests.

To confirm the LCN reusability, we performed cyclic testing on the 1 wt% TiO_2 sample. After the initial regeneration (black curve in Figure 4c), we performed again the whole deprotonation-adsorption-regeneration process three other times. The adsorption curves over the four cycles are reported in Figure S13, showing no consistent difference in adsorption capability over different cycles. This proves that the sorption capability of the sample is maintained over few photoregeneration cycles. After each adsorption, the samples were regenerated in the usual manner with spectra collected over time shown in Figure S14 and summarized in Figure 4c, with pictures of the sample after each adsorption/regeneration reported in Figure S15. The regeneration process remains long, with times of irradiation needed >15 h to get to equilibrium condition. The efficacy of regeneration drops slightly after the first cycles, getting to a stable value between the third and fourth cycles. The drop in regeneration capabilities is assigned to a partial degradation of the sample (observable by absorbance spectrum in the range of 400–450 nm, Figure S14). Even though it does not affect its adsorption capabilities.

We also assessed the external quantum efficiency (EQE) of the process which is defined as the ratio of molecules degraded per unit time over the photons absorbed by the system (see Section S4.1 and Figure S16) over subsequent cycles. The EQE values at the beginning of the exposure are reported in Figure 4d. Over different cycles, it drops from 0.3% to 0.14% and then stabilizes around 0.06%. The quantum efficiency over time is instead reported in Figure S17. Due to the limitation in concentration of the MB, methylene blue; occurring after the initial degradation, the quantum efficiency drops sharply after a few minutes, down to $<10^{-2}$%. Albeit lower, these final values are stable and on

the same order of magnitude of similar systems, confirming the possibility to reliably regenerate the samples.[39,50,66] This, joined with samples maintaining their capacity of adsorption and selectivity over different cycles, suggest the LCNs can be of practical reuse.

2.4 | Towards real wastewater treatment

To move towards a possible real application for wastewater purification, the best-performing sample (i.e., LCN loaded with 1 wt% TiO_2) was tested directly when immersed in water to mimic a wider range of conditions suitable for photo-regeneration and compared with a pristine LCN. After adsorption (Figure S18), the regeneration in water (Figure 5) shows a similar behavior to the one reported in air (Figure 4a), with concentration of MB, methylene blue; that drops consistently during the irradiation. This process allows us to avoid drying and washing steps and thus simplifies the regeneration protocol.

We also tested the efficacy of the system with a real pollutant beyond model dyes using the herbicide Diquat (a dicationic pollutant, inset of Figure 6a).[51,52] The LCN shows great adsorption capability, being able to adsorb up to 350 mg g^{-1} (Figure 6a). The sorption data are consistent with the Langmuir model, as shown by the fitting curve reported in the same figure. The lower q_L value compared to MB is assigned to the different charge and geometry and molecular weight of the two pollutant molecules: Diquat carries two positive charges and a smaller molecular weight, due to its molecular geometry, it is likely to interact planarly with the film and probably occupy or shield more active sites than MB, which has only one positive charge and can interact vertically or diagonally with the adsorbent surface.

Also in this case, the presence of TiO_2 allows for Diquat photodegradation, this time studied through photoluminescence. Indeed, because Diquat have an absorbance peak superimposed to the catalyst absorbance (Figure S19),[52] we monitored its fluorescence to assess the regeneration of the sample, while sorption was monitored as in the previous case (Figures S20 and S21). The normalized photoluminescence intensity dynamics over irradiation is reported in Figure 6b, where the regeneration appears about twice to three times faster than for MB and leads to a complete quenching of the emission signal in about 5 h. The degradation is confirmed by the absorbance spectra reported in Figure S22, where the Diquat absorbance peak is no longer detected after irradiation. While we exclude a consistent role of photobleaching as Diquat can last up to a week under direct sunlight (which carries around one fourth of the UV intensity we are using)[67,68] Diquat itself might be more sensitive to the photocatalysis process. This may be due to stronger interaction between Diquat and LCN matrix at the binding sites, as the adsorption tests suggested. Regarding the byproducts of Diquat degradation, Che et al. suggest that the degradation via ROS leads to pyrido-pyrazinium, pyridinyl, oxazolone, and methoxyoxo-methylium, ultimately mineralizing it into harmless carbon dioxide.[51]

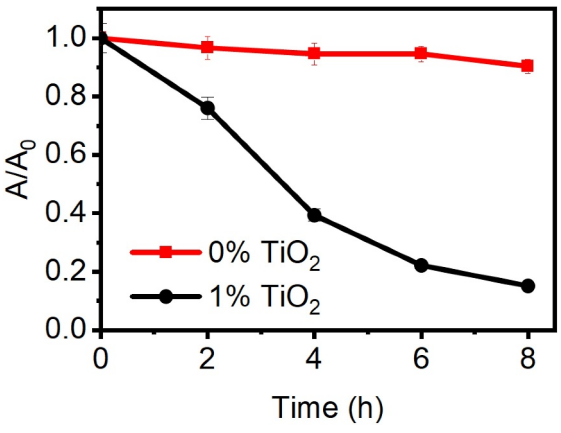

FIGURE 5 Normalized MB absorbance dynamics during photoregeneration of pristine LCN (red) and LCN loaded with 1 wt% TiO_2 (black) in water. LCN, liquid crystal network; MB, methylene blue.

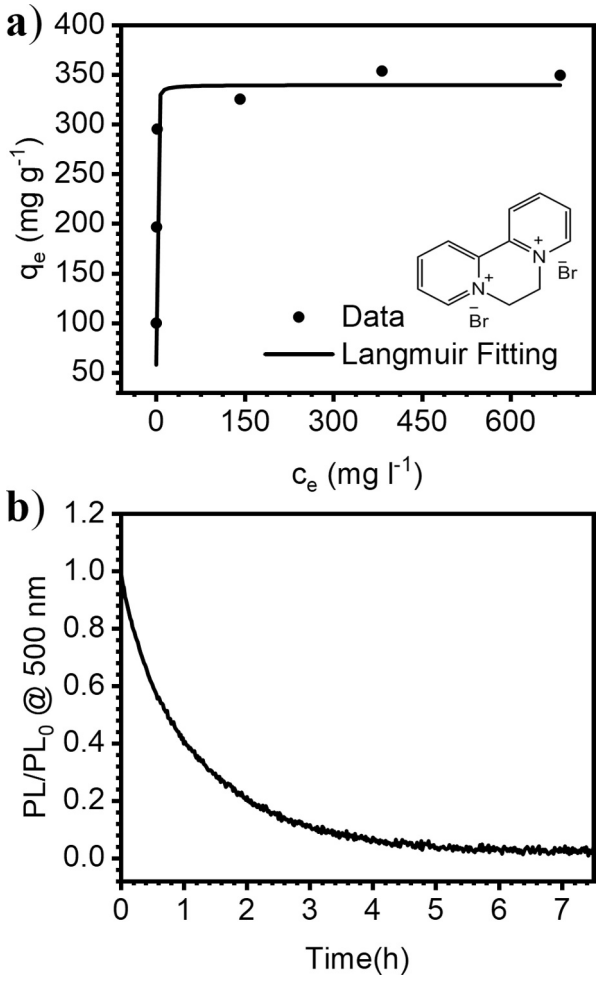

FIGURE 6 (a) Adsorption isotherm for 1% TiO_2-filled LCN film with Diquat. Solid line corresponds to the best fitting of the Langmuir model (Equation 1) to experimental data. (b) Normalized decrease of peak (~500 nm) Diquat photoluminescence intensity over irradiation time, extracted from Figure S21c. LCN, liquid crystal network.

2.5 | Comparison with literature results for MB, methylene blue; adsorption

The maximum adsorption capacities for MB, methylene blue; of different materials from literature are summarized in Table 1. For the sake of comparison, we focused on representative TiO_2-containing materials, irrespective of their form, that is, films, (nano)particles, monoliths, etc., that were expressly developed for adsorption and subsequent photocatalysis purposes.

Evidently, the adsorption capacity of the 1 wt% TiO_2-loaded LCN films developed in this work as reported in the previous sections is extremely high compared to most other materials proposed in the literature. In addition to performance values, we also highlight that working with macroscopic samples, here in the form of films, is significantly advantageous compared to using nanoparticles or powders in terms of ease of handling and separation from the liquid medium.

3 | CONCLUSION

The present work proposes photo-regenerable adsorbent films for cationic species in the form of LCN films obtained through photopolymerization of a commercial mesogen upon addition of TiO_2 nanoparticles as photocatalyst. The optimized formulation was the LCN film loaded with 1 wt% TiO_2 that can adsorb up to 747 mg g^{-1} of the dye MB or up to 350 mg g^{-1} of the herbicide Diquat. Thanks to the presence of TiO_2 nanoparticles, the samples can be regenerated from both the molecules upon light irradiation over the course of a few hours maintaining almost completely their adsorption capabilities. Upon subsequent regeneration tends to become less efficient, with external quantum efficiencies for the process degrading from 0.25% to a stable 0.05% over four cycles, still retaining the possibility for the adsorber to be regenerated and reused. Our results prove that liquid crystalline networks can be a promising steppingstone towards the goal of pollutants removal and water remediation.

4 | EXPERIMENTAL SECTION

4.1 | LC mixtures

LC mixtures were prepared by mixing 4-(6-acryloyloxyhexyloxy) benzoic acid (6OBA) and 1,4-phenylene bis(4-(6-(acryloyloxy)hexyloxy)benzoate) (C6H), by Synthon Chemicals, in a 90:10 weight ratio (Figure 2a,b). Irgacure 369 (0.5 wt%) was added as photoinitiator, along with 0.1 wt% of 2-methylbenzene-1,4-diol to inhibit thermal polymerization.[77] The mixture was dissolved in dichloromethane under sonication and then dried under reduced pressure. For the preparation of composites, Aeroxide® TiO_2 P25 nanoparticles by Evonik (nominally 3–99 nm particle size, from literature[78] 10–50 nm mainly 15–25 nm with surface area ~64 m^2/g) at 1, 5, and 10 wt% were dispersed in the solution and sonicated.

4.2 | Liquid crystal networks

Both pristine LCNs and TiO_2-LCN composites were fabricated via capillary infiltration, melting the LC mixture at 120°C between two glass slides separated by 40 μm-thick calibrated spacers (Thermo Scientific™, NIST 9000 Series). The slides were previously spun-cast (KLM SCC200 Spin Coater) with a 5 wt% aqueous solution of polyvinyl alcohol (PVA, Mw 89,000–98,000, 99+% hydrolyzed, Merck).

The films were photopolymerized at 95°C within the smectic phase, under UV irradiation (Thorlabs M385LP1-C4 LED, 23 mW cm^{-2}) for 10 min and then annealed at 120°C for 5 min.

Before the adsorption test, the films were activated with a 0.05 M KOH solution for 2 h (to allow H-bonding cleavage

TABLE 1 Comparison of the maximum adsorption capacity of the LCN loaded with 1 wt% of TiO_2 with literature data on other TiO_2-containing materials intended for the adsorption and photocatalysis of methylene blue.

Material	Sorption capacity [mg g^{-1}][a]	Refs
Titanium oxide−polyethylene glycol diacrylate hybrid microbeads	0.215	[69]
TiO_2 thin film modified with an Anderson aluminum polyoxometalate	27.4	[70]
Bentonite −20% TiO_2 composite powder	48.23	[71]
Graphene oxide/$ZnTiO_3$/TiO_2 composite powder	77.95	[72]
TiO_2/CuO/GO nanocomposite powder	79.57	[73]
TiO_2-based nanosheet modified Ag_2O (Ag/Ti atomic ratio = 5%)	172.4	[74]
TiO_2 coated polypyrrole composites	273.22	[75]
TiO_2 nanoparticle-containing hydrogel nanocomposite of polyacrylamide-grafted gum ghatti	1305.5	[76]
LCN 1 wt% TiO_2	750	This work

[a]Taken as equilibrium adsorption capacity (q_e) according to Langmuir fitting to experimental data.

and induce the presence of negatively charged sites) then washed in ethanol.[30]

4.3 | Characterization of LCNs

POM was conducted using a Zeiss Axio Observer A1 microscope equipped with cross-polarizers, a Linkam PE120 heating stage, and an Axio camera. ATR-IR spectra were acquired with a Spectrum Two spectrometer (PerkinElmer). Thermal transitions were analyzed using DSC (Q2000, TA Instruments) under N_2 atmosphere.

4.4 | Selectivity and adsorption isotherms

The adsorption behavior of pristine and TiO_2-loaded LCN was investigated through batch adsorption tests. First, selectivity was tested by using binary mixtures of dyes bearing opposite charge, that is MB + Methyl Orange and Rhodamine 6G + Indigo Carmine. Then, adsorption isotherms were measured by using aqueous solutions (pH ~ 6.8) containing different concentrations of pollutants, either MB or Diquat. For all experiments, the liquid to solid ratio 3 L g^{-1} and the samples were stirred at 300 rpm at 25°C in a thermostatic shaker (MTC-100, MIULAB) for 48 h. The adsorbed amount of dye was calculated based on the residual pollutant concentration in solution measured by using a UV-Vis spectrophotometer (UV-30, Honda). The equilibrium adsorption capacity (q_e) was calculated as described in Supporting Information S1.

4.5 | Photoregeneration

After adsorbing all MB from 5 mL of a 3.75×10^{-6} M solution of MB, samples were photoregenerated in air in an integrating sphere (Avantes Avasphere-50) equipped with a deuterium-halogen light source (AvaLight DH-S-BAL), a 365 nm LED (Luminus SST-10, 24 mW cm^{-2}) coupled to a 390 nm lowpass Filter (Semrock Brightline) and two spectrophotometers (Avantes ULS2048x64TEC-EVO and ULS4096CL-EVO) for detection. A microcontroller (Arduino Uno) synchronizes the opening and closing of two shutters via transistor-transistor logic signals. The sample is inserted in the sphere onto a fused silica window above the lower opening. Alternative activation of the shutters allows alternating the UV irradiation to white light. Closing the white light shutter, the first spectrophotometer collects the LED emission needed to calculate EQE. Vice versa, when the LED shutter closes, the second spectrophotometer takes white light absorbance measurement. For Diquat instead, after adsorbing from 3.5 mL of a 10^{-5} mL solution, photoluminescence was monitored instead of absorbance, placing the sample in the sphere and irradiating it with the LED. The sphere was coupled to a detector through a long pass filter (405 nm, Semrock Edgebasic) to measure the Diquat emission signal. Before and after the regeneration, the sample's absorbance in the UV region was measured with the integrating sphere with respect to a white reference (Avantes WS-2). The process quantum yield was assessed as described in Section S5 and Figure S16 for all regeneration experiments.

This test was also conducted by irradiating samples immersed in 1 mL of deionized water with an UWAVE LED UV lamp (365 nm, 24 mW cm^{-2}). Degradation was assessed with a UV–Vis spectrophotometer (Lambda 45, PerkinElmer) equipped with an integrating sphere.

ACKNOWLEDGMENTS

We acknowledge funding by the by the Italian Ministry of University and Research (MUR) through the project PRIN 2022 Wateronic—PRIN20227WZXJ3. The authors thank Dr. Sabrina Carroccio for the insightful discussions during the conception of the WATERONIC project.

CONFLICT OF INTEREST STATEMENT

The authors declare no conflicts of interest.

DATA AVAILABILITY STATEMENT

Data will be made available on request.

ORCID

Andrea Lanfranchi https://orcid.org/0000-0003-3642-2611

REFERENCES

1. J. Lubchenco, *Science* **1998**, *279*, 491.
2. M. Salgot, M. Folch, *Curr. Opin. Environ. Sci. Health* **2018**, *2*, 64.
3. M. N. Rashed, in *Organic Pollutants - Monitoring, Risk and Treatment* (Ed: M. N. Rashed), IntechOpen, Rijeka **2013**.
4. J. F. J. R. Pesqueira, M. F. R. Pereira, A. M. T. Silva, *J. Clean. Prod.* **2020**, *261*, 121078.
5. E. Eljarrat, D. Barceló, *TrAC, Trends Anal. Chem.* **2003**, *22*, 655.
6. *EU Commission, Circular Economy Action Plan*, https://ec.europa.eu/environment/circular-economy/pdf/new_circular_economy_action_plan.pdf (accessed: September 2025).
7. A. Castellano-Hinojosa, M. J. Gallardo-Altamirano, J. González-López, A. González-Martínez, *J. Hazard. Mater.* **2023**, *447*, 130818.
8. S. Domingo-Echaburu, L. M. Dávalos, G. Orive, U. Lertxundi, *Sci. Total Environ.* **2021**, *800*, 149412.
9. P. Wardrop, J. Shimeta, D. Nugegoda, P. D. Morrison, A. Miranda, M. Tang, B. O. Clarke, *Environ. Sci. Technol.* **2016**, *50*, 4037.
10. S. Bertucci, P. Lova, *Sol. RRL* **2024**, *8*, 2400116.
11. H. Kim, S. D. Kim, *Sci. Total Environ.* **2024**, *946*, 174388.
12. D. Cheng, H. H. Ngo, W. Guo, S. W. Chang, D. D. Nguyen, Y. Liu, Q. Wei, D. Wei, *J. Hazard. Mater.* **2020**, *387*, 121682.
13. T. Langenbach, in *Applied Bioremediation - Active and Passive Approaches* (Eds: Y. Patil, P. Rao), IntechOpen, Rijeka **2013**.
14. K. C. Khulbe, T. Matsuura, *Appl. Water Sci.* **2018**, *8*, 19.
15. K. K. Yadav, M. M. S. Cabral-Pinto, A. Gacem, A. M. Fallatah, B. Ravindran, S. Rezania, J. S. Algethami, L. Bashier Eltayeb, M. Abbas, T. Hassan Al-shareef, V. Vinayak, C. Truong Son, M. Awjan Alreshidi, J. Manuel Rodríguez-Díaz, R. Z. Homod, *Mater. Today Chem.* **2024**, *40*, 102226.
16. P. Vasudhevan, L. Shuhao, Z. Ruoyu, V. Manikandan, D. Yu, S. Devanesan, P. K. Sarangi, H. Ma, S. Dixit, S. Pu, *J. Environ. Chem. Eng.* **2025**, *13*, 115237.

17. D. B. Tripathy, A. Gupta, *Membranes* **2023**, *13*, 713, https://www.mdpi.com/2077-0375/13/8/713 (accessed: October 2025).
18. D. M. Stevens, J. Y. Shu, M. Reichert, A. Roy, *Ind. Eng. Chem. Res.* **2017**, *56*, 10526.
19. R. Song, J.-A. Lv, *Responsive Mater.* **2025**, *n/a*, e70022.
20. C.-Y. Lo, Y. Zhao, C. Kim, Y. Alsaid, R. Khodambashi, M. Peet, R. Fisher, H. Marvi, S. Berman, D. Aukes, X. He, *Mater. Today* **2021**, *50*, 35.
21. S. Ma, P. Xue, C. Valenzuela, Y. Liu, Y. Chen, Y. Feng, R. Bi, X. Yang, Y. Yang, C. Sun, X. Xu, L. Wang, *Adv. Mater.* **2025**, *37*, 2505018.
22. Y. Zhang, R. Liu, J. Chen, *Responsive Mater.* **2025**, *3*, e20250010.
23. Y. Xu, X. Zhang, Z. Song, X. Chen, Y. Huang, J. Wang, B. Li, S. Huang, Q. Li, *Angew. Chem. Int. Ed.* **2024**, *63*, e202319698.
24. Y. Xu, M. Jin, J. Wang, S. Huang, Q. Li, *Responsive Mater.* **2024**, *2*, e20240020.
25. J. Gao, Y. Tang, D. Martella, J. Guo, D. S. Wiersma, Q. Li, *Responsive Mater.* **2023**, *1*, e20230008.
26. H. K. Bisoyi, Q. Li, *Chem. Rev.* **2022**, *122*, 4887.
27. Y. Chen, C. Valenzuela, Y. Liu, X. Yang, Y. Yang, X. Zhang, S. Ma, R. Bi, L. Wang, W. Feng, *Matter* **2025**, *8*, 101904.
28. R. Lan, X.-G. Hu, J. Chen, X. Zeng, X. Chen, T. Du, X. Song, H. Yang, *Responsive Mater.* **2024**, *2*, e20230030.
29. M. Abad, A. Martínez-Bueno, A. Concellón, *Adv. Mater. Technol.* **2025**, *n/a*, e01236.
30. H. P. C. van Kuringen, G. M. Eikelboom, I. K. Shishmanova, D. J. Broer, A. P. H. J. Schenning, *Adv. Funct. Mater.* **2014**, *24*, 5045.
31. J. Kloos, N. Joosten, A. Schenning, K. Nijmeijer, *J. Membr. Sci.* **2021**, *620*, 118849.
32. D. Devadiga, A. TN, *Adv. Mater. Interfaces* **2022**, *9*, 2101276.
33. H. P. C. van Kuringen, Z. J. W. A. Leijten, A. H. Gelebart, D. J. Mulder, G. Portale, D. J. Broer, A. P. H. J. Schenning, *Macromolecules* **2015**, *48*, 4073.
34. T. Liang, H. P. C. van Kuringen, D. J. Mulder, S. Tan, Y. Wu, Z. Borneman, K. Nijmeijer, A. P. H. J. Schenning, *ACS Appl. Mater. Interfaces* **2017**, *9*, 35218.
35. S. Tian, S. J. D. Lugger, C.-S. Lee, M. G. Debije, A. P. H. J. Schenning, *J. Am. Chem. Soc.* **2023**, *145*, 19347.
36. Y. Foelen, R. Puglisi, M. G. Debije, A. P. H. J. Schenning, *ACS Appl. Opt. Mater.* **2023**, *1*, 107.
37. D. J. Mulder, L. M. W. Scheres, J. Dong, G. Portale, D. J. Broer, A. P. H. J. Schenning, *Chem. Mater.* **2017**, *29*, 6601.
38. S. Suárez, I. Jansson, B. Ohtani, B. Sánchez, *Catal. Today* **2019**, *326*, 2.
39. I. Jansson, S. Suárez, F. J. Garcia-Garcia, B. Sánchez, *Appl. Catal., B* **2015**, *178*, 100.
40. W. Yu, L. Zhang, H. Xu, H. Wang, X. Peng, S. Wu, W. Yang, J. Zhou, *Fuel* **2021**, *286*, 119427.
41. L. A. d. Silva, S. M. S. Borges, P. N. Paulino, M. A. Fraga, S. T. d. Oliva, S. G. Marchetti, M. d. C. Rangel, *Catal. Today* **2017**, *289*, 237.
42. S. Mazzanti, G. Manfredi, A. J. Barker, M. Antonietti, A. Savateev, P. Giusto, *ACS Catal.* **2021**, *11*, 11109.
43. B. Dauth, P. Giusto, B. König, R. M. Gschwind, *Angew. Chem. Int. Ed.* **2024**, *63*, e202412972.
44. C. Karthikeyan, P. Arunachalam, K. Ramachandran, A. M. Al-Mayouf, S. Karuppuchamy, *J. Alloys Compd.* **2020**, *828*, 154281.
45. M. Akkari, P. Aranda, H. Ben Rhaiem, A. Ben Haj Amara, E. Ruiz-Hitzky, *Appl. Clay Sci.* **2016**, *131*, 131.
46. D. Wang, Y. Ying, L. Cai, H. Cheng, S. Giannakis, G. Moussavi, Z. He, S. Song, J. Ma, *Chem. Eng. J.* **2025**, *516*, 163890.
47. A. Jamrah, H. Al-Jawaldeh, T. M. Al-Zghoul, A. Hamaideh, M. M. Darwish, E. Al-Karablieh, *Water Conserv. Manage.* **2024**, *8*, 415.
48. N. Bashir, T. Sawaira, A. Jamil, M. Awais, A. Habib, A. Afzal, *Mater. Today Sustain.* **2024**, *27*, 100869.
49. T. Zhou, G. Che, C. Liu, L. Ding, H. Teng, *Arab. J. Chem.* **2024**, *17*, 105808.
50. R. S. Pedanekar, S. K. Shaikh, K. Y. Rajpure, *Curr. Appl. Phys.* **2020**, *20*, 931.
51. G. Che, W. Yang, J. Luo, M. Li, X. Li, Q. Pan, *Sep. Purif. Technol.* **2024**, *334*, 126126.
52. S. H. Yuen, J. E. Bagness, D. Myles, *Analyst* **1967**, *92*, 375.
53. H.-Q. Chen, X.-Y. Wang, H. K. Bisoyi, L.-J. Chen, Q. Li, *Langmuir* **2021**, *37*, 3789.
54. J. W. Goodby, G. W. Gray, in *Handbook of Liquid Crystals* (Eds: D. Demus, J. W. Goodby, G. W. Gray, H. W. Spiess, V. Vill), Vol. III, Wiley, NY, USA **1998**.
55. D. Dunmur, K. Toriyama, in *Handbook of Liquid Crystals* (Eds: D. Demus, J. W. Goodby, G. W. Gray, H. W. Spiess, V. Vill), Vol. III, Wiley, NY, USA **1998**.
56. M. J. Stephen, J. P. Straley, *Rev. Mod. Phys.* **1974**, *46*, 617.
57. D. Martella, M. Mannelli, R. Squecco, R. Garella, E. Idrizaj, D. Antonioli, M. Laus, D. S. Wiersma, T. Gamberi, P. Paoli, C. Parmeggiani, T. Fiaschi, *iScience* **2021**, *24*, 103077.
58. P. Simova, N. Kirov, M. P. Fontana, H. Ratajczak, *Atlas of Vibrational Spectra of Liquid Crystals*, World Scientific Publishing, Singapore **1988**.
59. H. Swenson, N. P. Stadie, *Langmuir* **2019**, *35*, 5409.
60. S. P. Yadav, R. Manohar, S. Singh, *Liq. Cryst.* **2015**, *42*, 1095.
61. S. Hao, Z. Jia, J. Wen, S. Li, W. Peng, R. Huang, X. Xu, *Sep. Purif. Technol.* **2021**, *255*, 117772.
62. F. Yang, P. Yang, *Macromol. Rapid Commun.* **2022**, *43*, 2100669.
63. A. Mills, J. Wang, *J. Photochem. Photobiol., A* **1999**, *127*, 123.
64. D. P. DePuccio, P. Botella, B. O'Rourke, C. C. Landry, *ACS Appl. Mater. Interfaces* **2015**, *7*, 1987.
65. X. Yan, T. Ohno, K. Nishijima, R. Abe, B. Ohtani, *Chem. Phys. Lett.* **2006**, *429*, 606.
66. N. Serpone, *J. Photochem. Photobiol., A* **1997**, *104*, 1.
67. H. H. Funderburk Jr., N. S. Negi, J. M. Lawrence, *Weeds* **1966**, *14*, 240.
68. P. Slade, A. E. Smith, *Nature* **1967**, *213*, 919.
69. M. Chen, Z. H. Farooqi, G. Bolognesi, G. T. Vladisavljević, *Langmuir* **2023**, *39*, 18784.
70. F. Duran, C. Diaz-Uribe, W. Vallejo, A. Muñoz-Acevedo, E. Schott, X. Zarate, *ACS Omega* **2023**, *8*, 27284.
71. L. Laysandra, M. W. M. K. Sari, F. E. Soetaredjo, K. Foe, J. N. Putro, A. Kurniawan, Y.-H. Ju, S. Ismadji, *Heliyon* **2017**, *3*, e00488.
72. X. Jaramillo-Fierro, G. Cuenca, *Int. J. Mol. Sci.* **2024**, *25*, 4367.
73. V. Rangel-Contreras, O. Reyes-Vallejo, V. Subramaniam, *J. Mater. Sci. Mater. Electron.* **2024**, *35*, 1301.
74. F. Chen, Z. Liu, Y. Liu, P. Fang, Y. Dai, *Chem. Eng. J.* **2013**, *221*, 283.
75. J. Li, J. Feng, W. Yan, *Appl. Surf. Sci.* **2013**, *279*, 400.
76. H. Mittal, S. S. Ray, *Int. J. Biol. Macromol.* **2016**, *88*, 66.
77. M. Turriani, N. Cosottini, N. Fuochi, D. S. Wiersma, D. Martella, C. Parmeggiani, *Soft Matter* **2025**, *21*, 1162.
78. M. Náfrádi, T. Alapi, L. Farkas, G. Bencsik, G. Kozma, K. Hernádi, *Materials* **2022**, *15*, 49.

SUPPORTING INFORMATION

Additional supporting information can be found online in the Supporting Information section at the end of this article.

How to cite this article: V. D'Agostino, V. Spinoso, G. Curcuruto, A. Longo, A. Martinez-Bueno, A. Lanfranchi, C. Laferrera, G. Impellizzeri, P. Lova, M. S. Luna, D. Martella, *Responsive Mater*. **2025**, e70027. https://doi.org/10.1002/rpm2.70027